P1.42   **THE IMPACT OF SIMULATED HIGH-RESOLUTION SURFACE OBSERVATIONS FOR CONVECTIVE STORMS WITH ENSEMBLE KALMAN FILTER**

Jili Dong*, Ming Xue, and Kelvin Droegemeier
School of Meteorology and Center for Analysis and Prediction of Storms
University of Oklahoma, Norman, OK 73072

1. Introduction

Successful numerical weather prediction (NWP) depends greatly on accurate initial conditions obtained with data assimilation. For convective storms, radar is the primary observational platform. However, radars usually do not observe down to the ground surface, because of the non-zero elevation of the lowest scans. This problem becomes worse as the storm is far away from the radar because of the beam elevation and the earth curvature effect. For example, when a storm is 100 km away from the radar, the center of the 0.5° elevation beam of the WSR-88D radar is more 2 km above the ground. Even the lower edge of the half power beam does not reach ground. Yet, for convective systems, the low-level flows and cold pool are of critical importance for the storm development and evolution. At the ground surface, observations from automated meteorological stations and some times from mesoscale observational networks are available. Effective assimilation of these observations, in combination with the radar data, has the potential to significantly improve the storm analysis and forecast

The assimilation of the surface observations into NWP models is not as easy as it might appear. One of the issues is with the often differing elevation of the surface observations and the model ground level. Complex terrains also make the spatial representativeness of the observations a complicated issue, which affects the proper spatial spreading of observation increments (Lazarus et al. 2002; Deng and Stull 2007). A more general issue is with the vertical spread of the observation information which in non-trivial because of the typically large spatial and temporal variations of the boundary layer structures. To optimally assimilate surface observations, flow dependent background error covariance is needed. The ensemble Kalman filter method (Evensen 2003) is a method that evolves flow-dependent error covariance through assimilation cycles by using ensemble forecasts.

* Corresponding author address:
Jili Dong, School of Meteorology,
National Weather Center, Suite 5900,
120 David L. Boren Blvd, Norman, OK 73072,
jldong@ou.edu

The assimilation of surface observations for the planetary boundary layer using EnKF has been examined recently, for simple column model settings with simulated and real observations (Hacker and Snyder 2005; Hacker and Rostkier-Edelstrein 2007). Simulated surface observations have also been tested with a mesoscale model for a synoptic scale winter cyclone case by Zhang et al. (2006) and Meng and Zhang (2007). Fujita et al. (2007) examined the performance of EnKF for synoptic-scale flows with real surface observations. The assimilation of high-resolution surface observations, from e.g., a high-density mesonet, for the initialization of explicit convective storms, is, however, limited to the study of Zhang et al. (2004), which found positive impact of surface observations of 10 km spacings when radar data were artificially limited to above 4 km level. This study also assumed that radar observations are available at the model grid points.

For the prediction of convective initiation and its later evolution, Liu and Xue (2007) show that the strength of an analyzed cold pool is sensitive to the vertical correlation length scale specified in the ARPS Data Analysis System (ADAS, Brewster 1996) when analyzing high-resolution surface observations including Oklahoma Mesonet data. Similar sensitivity was found by Dawson and Xue (2006). Within ADAS, the vertical correlation length can be specified in terms of the geometric height or potential temperature. The latter would allow more vertical spreading of observation information in less stable conditions but the correlation scale is still empirical. Using ADAS and observations from regular and various local mesoscale surface networks that were gathered by the IHOP (Weckwerth et al. 2004) project, Liu and Xue (2007) showed significant positive impact of 6-hour-long hourly assimilation cycles on improving convective initiation forecast in the ARPS model. Similar was found by Xue and Martin (2006) using a 6-hourly assimilation cycle for another convective initiation case from IHOP.

In this study, we set out to perform a systematic study on the impact of assimilating high-resolution observations from a hypothetical surface mesonet, in addition to observations from a relatively distant radar that do not cover the low levels of the atmosphere. The true WSR-88D radar scanning mode is used, providing a realistic data coverage. The mesonet stations are assumed to be uniformly distributed for easier interpreta-

tion of results, and different station spacings are examined. The impact of the surface data is interpreted in terms of the expected impact on convective storm simulation and prediction.

The rest of this paper is organized as follows. Section 2 describes the numerical model, the design of observational network and the EnKF algorithm used. Experiments assimilating surface observations with EnKF are shown in section 3 and sensitivity tests are shown and analyzed in section 4. The impact on subsequent forecast is discussed in section 5. Section 6 provides an overall summary.

2. Model and Experiment Settings

We take the Observing System Simulation Experiment (OSSE, Lord et al. 1997) approach in this study, as most of existing EnKF studies do. With OSSEs, a model simulation is first created, which serves as the 'truth' or 'nature run' for the experiments. Realistic observations can be simulated from this model atmosphere, using, e.g., a radar simulator for radar data (e.g., Jung et al. 2007), and by assuming certain surface network characteristics for surface observations. With OSSE, observation configurations currently unavailable can be tested. This study builds upon and extends the earlier OSSE studies of Tong and Xue (Tong and Xue 2005, TX05 hereafter) and Xue et al. (2006, XTD06 hereafter).

a) Description of simulation and assimilating model

The Advanced Regional Prediction System (ARPS, Xue et al. 2000; Xue et al. 2001; Xue et al. 2003) is used as the simulation and prediction model in this study. The ARPS is a fully compressible and nonhydrostatic model that predicts three velocity components u, v, w, potential temperature θ, pressure p, the mixing ratios for water vapor, cloud water, rainwater, cloud ice, snow, and hail/graupel (q_v, q_c, q_r, q_i, q_s, and q_h, respectively) associated with the ice microphysics scheme. The variables make up the state vector that is estimated or analyzed using EnKF. The model also predicts the turbulence kinetic energy (TKE) which is used by the 1.5-order subgrid-scale turbulence closure scheme. TKE is not updated by the EnKF during the assimilation cycles. The ARPS includes several single-moment ice microphysics packages. The Lin et al. (1983, LFO83 hereafter) scheme is the default and is used in this study.

As in TX05 and XTD06, the 20 May 1977 Del City, Oklahoma, supercell storm (Ray et al. 1981) simulated by the ARPS is used as the truth for the OSSEs. A horizontal resolution of 2 km is chosen with a grid of $67 \times 67 \times 35$ points in x, y and z direction, respectively, giving a physical domain of 128 × 128 × 16 km (the model defines extra points outside the physical boundary). Radar and surface observations are assumed to be available only within a 64 × 64 km subdomain located at the center of the model grid. The main storm cells remained within this subdomain for the length of the assimilation and prediction, and this observation domain has the same size as that used by TX05. In the vertical, a grid stretching scheme based on a hyperbolic tangent function is used and the vertical grid spacing is 200 m near the ground and increases 800 m at the model top.

An initial thermal bubble with a maximum perturbation of 4 K is centred at x = 80 km, y = 48 km and z = 1.5 km to initialize convection. The radii of the bubble are 10 km in horizontal and 1.5 km in vertical. Open lateral boundary and free-slip bottom boundary conditions are used in both simulation and assimilation. A constant wind of u = 3 m s^{-1} and v = 14 m s^{-1} is subtracted from the original sounding to keep the storm near the center of the domain. These configurations are the same as those used in TX05, except for the large computational domain and the use of vertical grid stretching here.

The bubble-triggered storm reached its full intensity before 30 min. At around 60 minutes, the supercell starts to split into two, one right mover and one left mover (Fig. 1.a). By 120 min, the left mover is exiting the northwest corner of the central subdomain (Fig. 2.a). Additional details on the general evolution of the ARPS simulated Dell City storm can be found in TX05 and Xue et al. (2001). The simulated model state is output every 5 min. for observation simulation and analysis/forecast verification purposes.

b) Simulation of observations

An hypothetical WSR-88D radar with 10 cm wavelength is located southwest of the storm, at x = -68 km and y = -68 in terms of the model coordinates, with a distance of about 185 km from the domain center where the right-moving cell is approximately located. At this distance, the earth curvature effect combined with the beam bending, based on the ¾ earth radius model (Doviak and Zrnic 1993) places the lower edge and the center of the half-power beam of 0.5 degree elevation at 1.98, 3.60 km above ground, respectively, at this distance. In another word, there is no direct radar data coverage below 1.98 km level at all at this distance.

Table 1: List of experiments under perfect model assumption

Experiment	Obs. Type	Sfc. Obs. Spacing (km)	Radar Dist. (km)	Remark
RA/CNTL	Radar only	N.A.	185	Control Exp.
RASFC	Radar+Sfc All	20	185	Control + Sfc. Data
RASFCUV	Radar+Sfc V	20	185	Single Sfc. Obs Comp. Tests
RASFCT	Radar+Sfc T	20	185	
RASFCP	Radar+Sfc Pres	20	185	
RASFCQV	Radar+Sfc Qv	20	185	
RASFCS12	Radar+Sfc All	12	185	Sfc Obs Spacing Tests
RASFCS6	Radar+Sfc All	6	185	
RAD115	Radar	N.A.	115	Radar Dist. Tests
RASFCD115	Radar+Sfc All	20	115	
RASFCD115S6	Radar+Sfc All	6	115	
RASFCD45	Radar+Sfc All	20	45	
RASFCD45S6	Radar+Sfc All	6	45	

As in XTD06, radar data are assumed to be available on the elevation levels in the vertical and already interpolated to model grid in the horizontal. The standard WSR-88D precipitation scanning mode is assumed (see Fig. 2 of XTD06). Radial velocity (V_r) is simulated the same way as in XTD06, and the same V_r observation operator is used in the EnKF assimilation. The reflectivity formula described in Tong and Xue (2005) is used for the simulation and assimilation. This formula returns the reflectivity (Z) in dBZ from the mixing ratios of rain, snow and hail/graupel.

Gaussian-distributed random errors with zero mean and standard deviations of 1 m s^{-1} and 3 dBZ are added to the simulated radial velocity and or reflectivity. The 3 dBZ standard deviation of reflectivity error is smaller than the 5 dBZ used in TX05 and XTD06, but is used in Tong and Xue (2007) and is shown by Xue et al. (2007) to be more appropriate. The larger error results in a slightly worse analysis.

Surface stations of an assumed mesoscale network are located inside the 64 × 64 km interior subdomain with a uniform station spacing of 20 km in control experiment therefore there are 9 stations altogether. The horizontal wind components, temperature, pressure and water vapor mixing ratio are the observed variables. The standard deviation of the zero-mean Gaussian errors added to the simulated station values are: 1 m s^{-1} for wind components, 1 K for temperature, 1 hPa for pressure and 1 g kg^{-1} for water vapor mixing ratio. The surface data are assumed to be available at the scalar grid points. Different station spacings are tested in sensitivity experiments.

Both radar and surface observations are assumed to be available every 5 minutes.

c) EnKF algorithm

The EnKF algorithm used in this study origins from Whitaker and Hamil (2002) which is a serial ensemble square root filter. The implementation follows XTD06 exactly, except for the addition of surface observations, which are assimilated after the radar data every 5 minutes.

In this study, the state variables updated include u, v, w, θ, p, q_v, q_c, q_r, q_i, q_s, and q_h. To initialize the first ensemble forecast cycle, random initial perturbations as used in XTD06 are added to a first guess defined as horizontally homogenous using the May 20 sounding of the truth simulation. The random perturbations are drawn from a Gaussian distribution with zero mean and standard deviations of 2 m s^{-1} for u, v, w, 2 K for potential temperature θ, and 0.6 g kg^{-1} for q_v and all microphysical variables. Perturbations for all variables except for microphysical variables are added to the entire subdomain. The perturbations for latter are added only in the region where there is radar echo at 25 minutes, the model time from which the assimilation cycles start. Reflectivity data in both precipitation and clear air region (negative reflectivity values are set to zero) are used. And for radial velocity only data in $Z \geq 10\,\mathrm{dBZ}$ region are used.

Covariance localization (Houtekamer and Mitchell 2001) is used to limit the influence of every observation. Schur product is applied with a smooth 5th-order function (Eq.(4.10) of Gaspari and Cohn, 1999) multiplying the calculated background error covariance. For radar observations, a 6-km cutoff radius in all direction is chosen to ensure a best result when only radar data is used (XTD06). For surface observations, when the sta-

tion spacing is 20 or 12 km, a horizontal cutoff radius of 24 km and a vertical radius of 6 km are found to be optimal. When the station spacing is 6 km, horizontal cutoff radii of 18 km and 6 km are used in the horizontal and vertical, respectively. Forty ensemble members are used for all experiments, as in XTD06

To avoid the filter divergence problem caused by covariance underestimation due to the small sample size and/or model error, covariance inflation is used in all experiments following the procedure of XT05. For cases using radar observations only, covariance inflation is only applied in and near (within 6 km of) the region where observed reflectivity exceeds 10 dBZ. In control experiments with only radar observations, a 5% inflation is applied. For experiments including surface observations, covariance inflation is also applied at the levels within the cut off radius of surface observations, in the entire subdomain, using the same inflation factor as for radar data.

d) Assimilation experiments

All of experiments performed in this paper assume a perfect assimilating model. They are listed in Tables 1. In the experiment names, 'RA' denotes the use of radar data, 'SFC' indicates the use of surface data, 'D' followed by a number indicates the radar distance, and 'S' followed by a number indicates surface station spacing. For example, RASFCD115S6 means that both radar and surface data are used and the radar is located 115 km from the domain center and the surface station space is 6 km.

The perfect-model results will be reported in the next three sections. We will focus on examining the impact of additional surface observations.

3. Impact of surface observations as compared to control experiment

The control experiment with radar data only (RA or CNTL, Table 1) is first performed as a benchmark for investigating the impact of surface observations. For most of these runs, the radar is located 185 km from the center of grid (Table 1). Fig. 1 shows the results of truth simulation and of experiments RA and RASFC, which adds data from a surface network of 20 km spacing. The ensemble mean analysis fields are plotted. At 60 min, or after either 35-minute analysis cycles, precipitation and cold pool associated with the storm are established in both RA and RASFC (Fig. 1c, e) but RA did not capture the splitting of the cell and the appearance of the left cell at this time. The cold pool is too broad in RA based on the -1 K θ contour but is a little too narrow in RASFC. RA almost completely missed the sur-

face wind convergence and the convergence center associated with main updraft is too weak and does not have the right pattern (Fig. 1d). In comparison, RASFC did a much better job capturing the convergence pattern along the gust fronts on the south and north side, and reproduces the magnitude and pattern of the main convergence center much better (Fig. 1f). In both cases, the analyzed fields are not very accurate at this time.

At 90 min (not shown), the right and left moving cells as seen from the low-level reflectivity are now reasonably captured in both cases. However, the convergence field is still not accurately analyzed, especially along the gust front. The convergence zone along the northwest boundary of cold pool, which is too weak in RA, is much better analyzed in RASFC in terms of both location and strength (not shown). By 120 min (Fig. 2), the hook echo structure of the major storm is reproduced well in both RA and RASFC (Fig. 2c, e). Again, there are more differences in the analyzed surface divergence fields. Both the intensity and pattern of the divergence from RASFC are reproduced accurately in RASFC (Fig. 2f), but that in RA is generally broader and the weaker tail at the southwest end is missing. Also missing is the convergence center associated with the left mover near the northwest corner of the domain (Fig. 2b).

The size of the cold pool is not better analyzed, as indicated by the -1 K θ contour. The θ gradient along the cold pool boundary is too weak, however, and there are also larger differences in the θ field near the western boundary and the northern boundary. At this time, the level analysis of RASFC can be considered very good (more quantitative measures of the analysis will be presented later).

From the comparison between RA and RASFC, it is clear that the surface station observations have a noticeable impact on the analysis of cold pool and its associated flow field, even through they have a resolution much coarser (~20 km) than needed to resolve the sharp gradient along the gust fronts. The impact on the precipitation field seems to be smaller, presumably because that the hydrometeors that descend to the ground level are well captured by the radar data above. Without surface data, we have to rely on the model to establish the cold pool through evaporative cooling. As the cold air spreads away from the precipitation region, no more radar data (except for zero reflectivity information) is available. We note here that since our experiments start relatively early during the life cycle of the bubble-triggered storm, the model is able to do a reasonable job in establishing the cold pool. If the assimilation is started much later when the cold pool is more wide spread, it will be much harder without the help of surface observations.
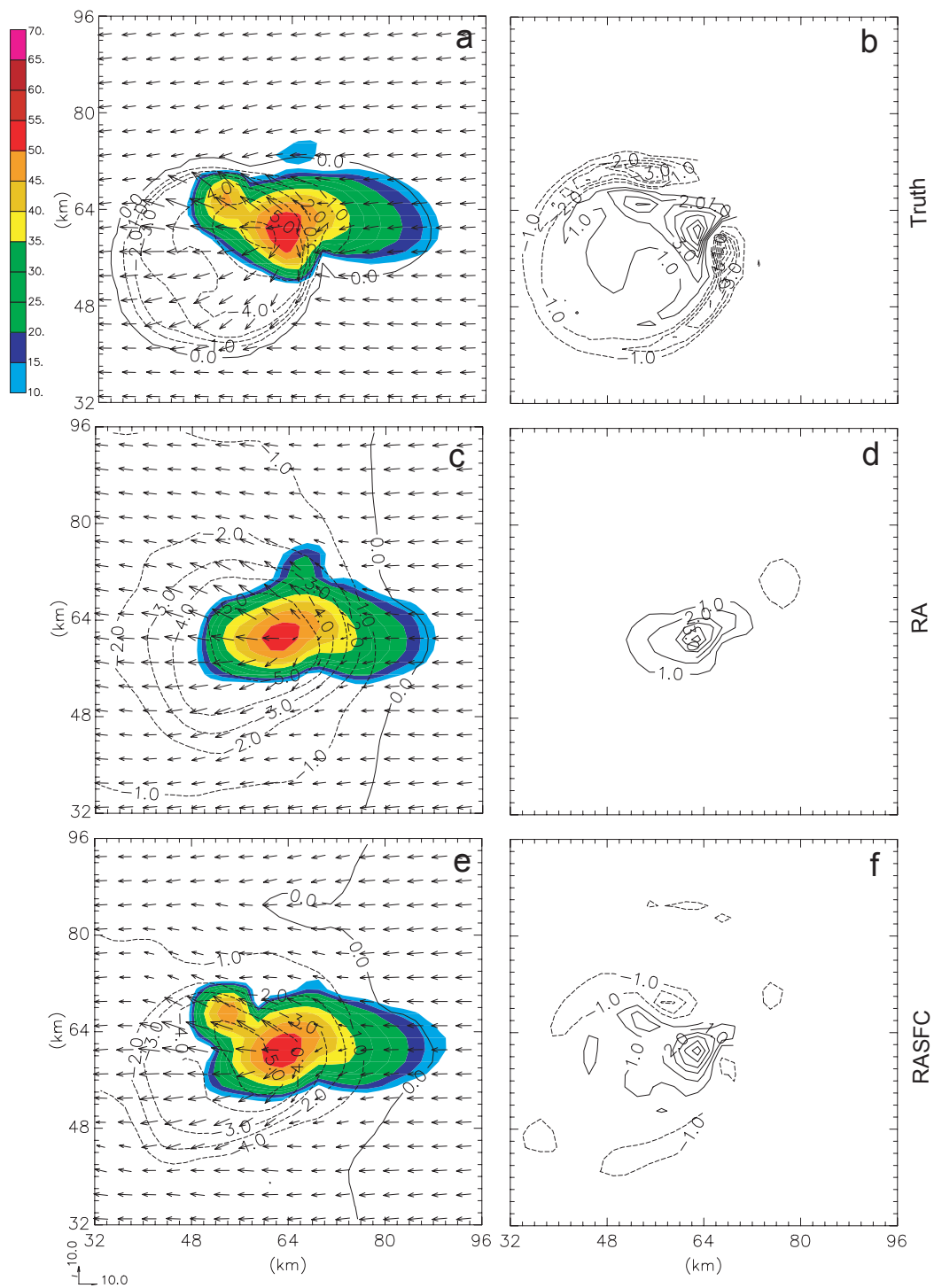
4

Fig. 1. Perturbation wind vector, simulated reflectivity Z (dBZ) and perturbation potential temperature θ' (K) (a, c, e), divergence field ($\times$ 1000 s^{-1}) (b, d, f) at z = 100 m (first model level above ground) for truth (a, b), and experiments RA (c, d) and RASFC (e, f) at 60 min.
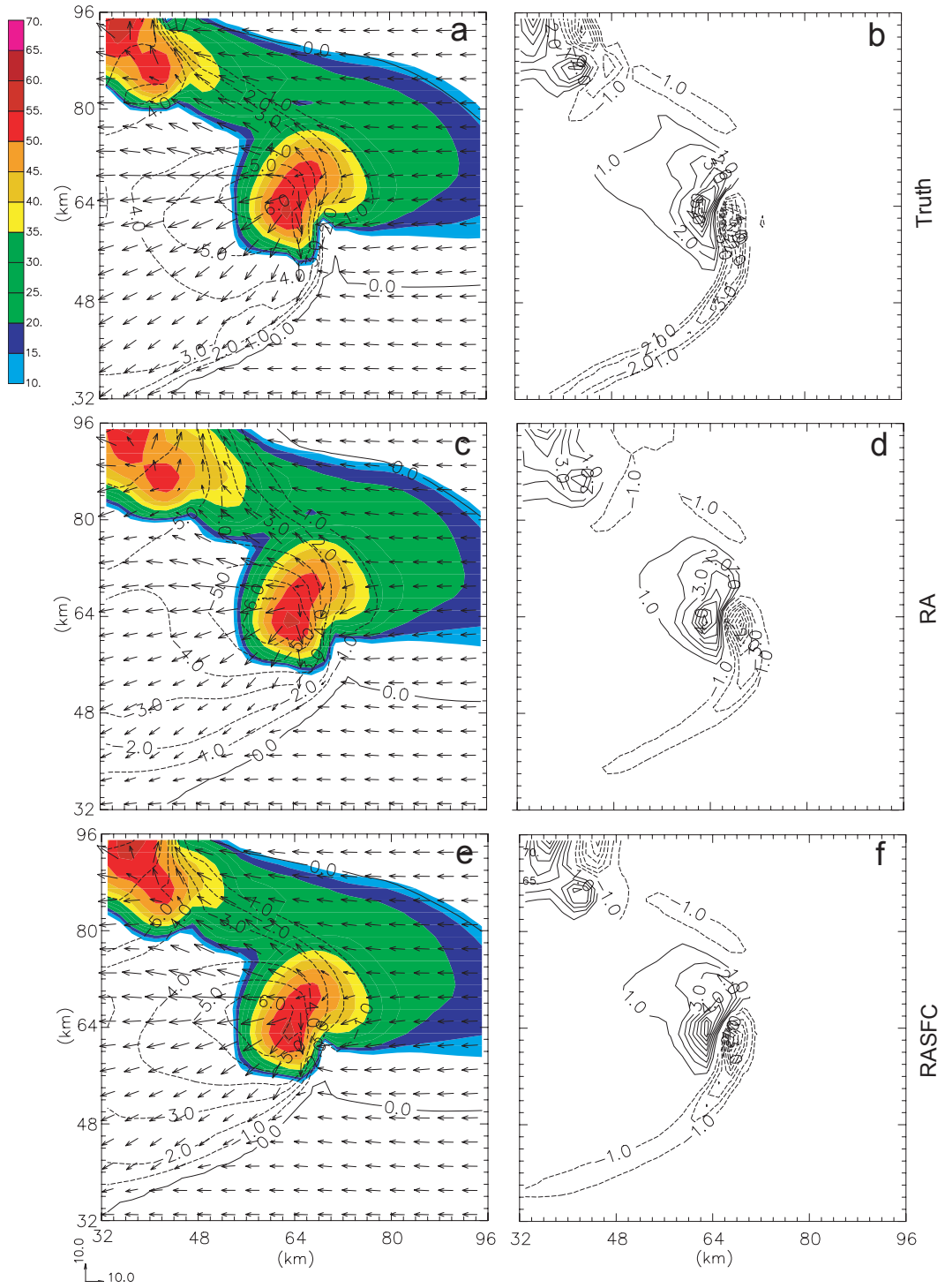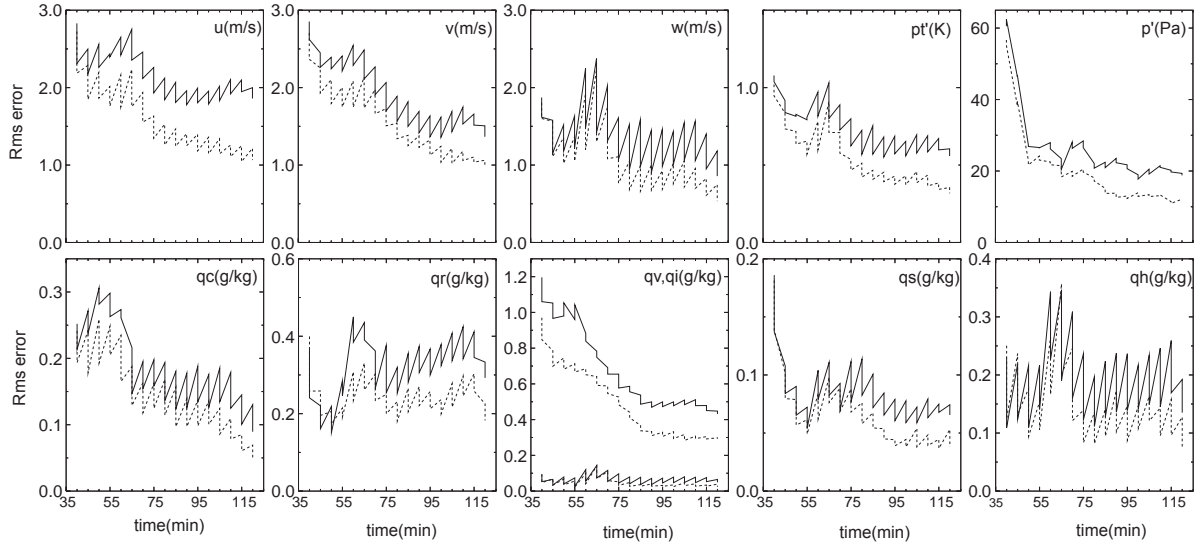
Fig. 2. As Fig. 1, but at 120 min.

Fig. 3. The rms error of ensemble mean forecasts and analyses plotted against time for RA (solid) and RASFC (dotted) for a) u, b) v, c) w, d) perturbation potential temperature θ', e) perturbation pressure p', f) q_c, g) q_r, h) q_v and q_i, i) q_s, j) q_h. The sharp reduction in the errors at the analysis times is due to the analysis update. See TX05 for further explanations on this type of plots if needed.
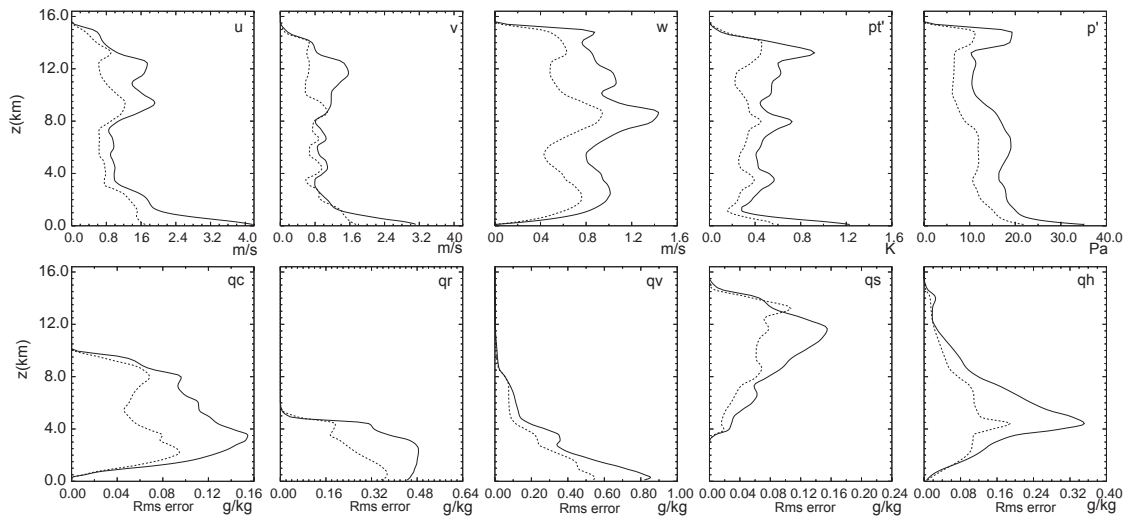

Fig. 4. The rms error profiles of ensemble mean analysis of RA (solid) and RASFC (dotted) for a) u, b) v, c) w, d) θ, e) p, f) q_c, g) q_r, h) q_v and q_i, i) q_s, j) q_h at 120 min.

Root mean square (*rms*) error of the ensemble mean analysis calculated against the truth is used to quantify the EnKF performance and the impact of surface data. The evolution of *rms* errors with time is shown in Fig. 3. As in TX05, the errors were calculated at grid points where observed Z exceeds 10 dBZ. The errors decrease during the first few cycles, from the initially very high level associate with the poor initial guess based on a single sounding. Errors starting from 40 min are shown.

It can be seen that at the end of assimilation, at 120 min, the errors in most fields are clearly lower in RASFC than in RA. The improvement due to surface data is largest in u and θ', with the errors in RASFC case being only about 57% those of RA. The absolute *rms* error reduction in RASFC is 0.8 ms^{-1} for u and 0.24 K for θ. Other variables also display improvements to various extent. The *rms* error in RASFC is 71% of RA for v, 62% of RA for w, and 65% and 68%

7

for pressure and q_v, respectively. Even for microphysical variables which are not directly observed by surface observations, the results also show significant improvements: the *rms* error is 54% of RA case for q_c, 62% for q_r, 50% for q_i, 58% for q_s and 56% for q_h. This says that there are 30% to almost 50% reduction in errors in various model fields due to the use of surface observations. We note that there are temporary increases in the rms error near 65 min, this happens in our earlier studies for this storm also (TX05 and XTD06) and is believed to related to the cell splitting at this time. To examine the impact of surface data at the upper level, vertical profiles of rms errors there were horizontally averaged over the precipitation regions are plotted in Fig. 4 for 120 min. Rms errors for u, v, θ, p, q_r, and q_v are largest at the low levels and near the surface in RA, becaused of the lack of low-level radar data. The largest improvements in RASFC are also found with these variables at the surface. For example, the rms error reductions are 2.4 ms^{-1} for u, 0.6 K for θ and 13 Pa for p at the surface, reflecting the better analysis of surface cold pool with the use of surface observations. For w and all four microphysical variables (q_c, q_r, q_s and q_h), the largest rms error reduction is found at the levels where the corresponding RA errors are largest. For example, the q_h error is reduced from about 0.35 to about 0.18 g kg^{-1} at about 4 km level and maximum reduction in q_s error at close to 12 km level is about 0.8 g kg^{-1}. The error reduction in w is mostly between 0.3 and 0.8 m s^{-1} between 2 and 13 km levels. The general improvement of the storm analysis at the upper levels away from the ground is very encouraging.

4. Sensitivity experiments with surface measurement type and spacing and radar location

a) Varying surface measurement type

In this section, the measurement types within the available surface observations, including wind, temperature, pressure and water vapor, are analyzed individually to assess their individual impact on the overall storm analysis. These experiments are listed as RASFCUV, RASFCT, RASFCP and RASFCQV in Table 1.

The *rms* errors for these four experiments shown in Fig. 5 indicate that for most state variables the surface wind observations have the largest impact while temperature observations have the second largest impact. Among all the surface observations, pressure observations have the least impact. In fact, the impact of pressure observations is minimal since the *rms* error curves of RASFCP are only slightly lower (e.g., by about 0.1 –

0.2 ms^{-1} for u, v and w) that those of RA shown in Fig. 3 For q_c, q_r and q_s, temperature observations result in smallest rms errors at the end of the assimilation cycles (120 min) but at other times their impact are close to or slightly smaller than that of wind. None of these individual measurements were able to produce as large an impact as RASFC, where all variables in the surface observations are assimilated. The errors of RASFCUV and RASFCT are very close to those of RASFC, however.

It is noticed that the largest improvements for state variables θ, p and q_v are obtained when assimilating surface winds rather than their direct measurement. This seems to be because that the rms errors for θ, p and q_v in RA are already reduced during the later cycles to values (Fig. 3) that are much smaller than the standard deviations of surface observations errors, which were specified to be 1 K for temperature, 100 Pa for pressure and 1 g kg^{-1} for q_v. Such error-containing observations have a limited ability to further reduce the errors of the corresponding state variables (however, keep in mind that the errors in θ, p and q_v are larger than those of domain means shown in Fig. 3 so some benefit still exists). For u and v, the analysis errors are still relatively large (Fig. 3 compared to the surface wind observation errors, which provides more room for the direct impact by the wind observations. When the wind observations are improved, other variables benefit too. In general, u, v and θ benefit most from the surface observations of wind and temperature. This is consistent with the fact the most important features at the surface as associated with the cold pool and its circulations. The hydrometeor fields are impacted less for the reasons stated earlier.

The fact the impact of surface observations is largest when all of the measured variables are assimilated is expected since in this case, every individual measurement is showing incremental benefit. The total impact using all measurements is smaller than the sum of individual impacts, in terms of the error reduction though. In summary, the surface wind observations are found to have the largest impact on the analysis of this particular storm. The improvement of cold pool analysis comes not only from thermodynamic observations, but even more so from wind observations, which directly improves the analysis of convergence and divergence patterns that are closely linked to updraft lifting and downdraft intensity. We do want to point out that the EnKF analysis is multivariate, and through cross-covariances derived from the ensemble, wind observations are used to update all state variables, not just wind components themselves.
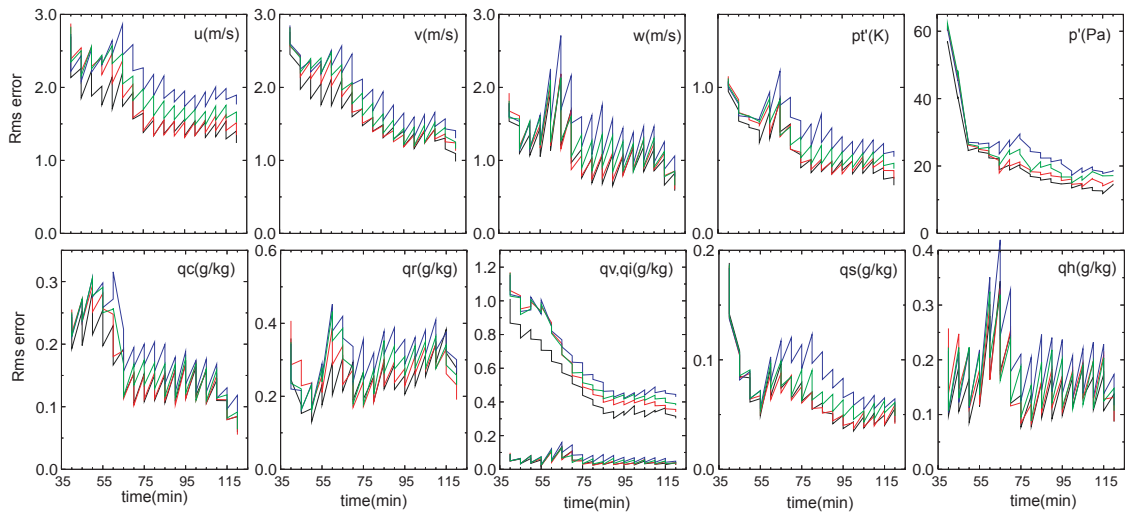
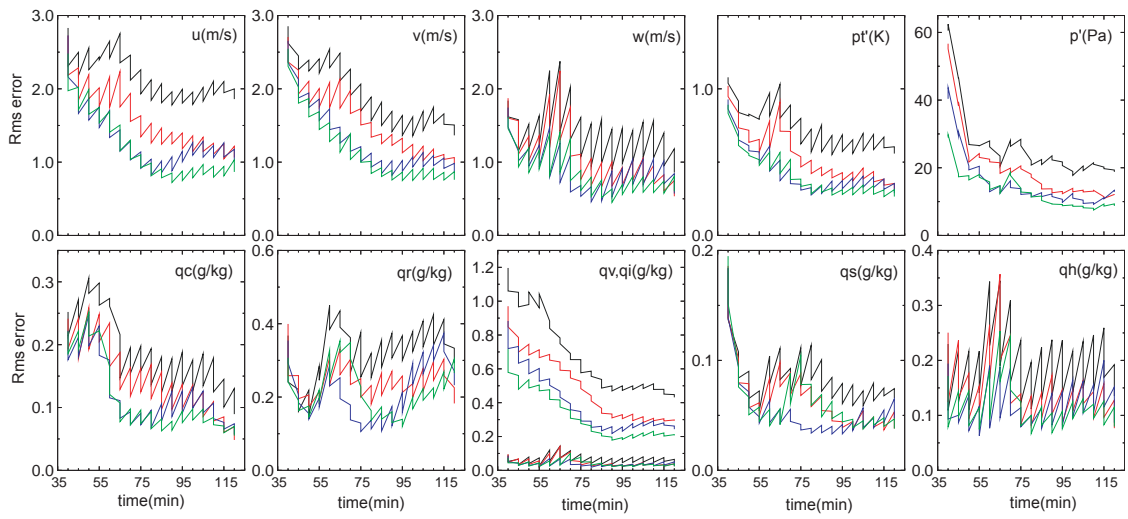Fig. 5. As Fig. 3, but for RASFCUV (black), RASFCT (red), RASFCP (blue) and RASFCQV (green).

Fig. 6. As Fig. 3, but for RA (black), RASFC (red), RASFCS12 (blue) and RASFCS6 (green).
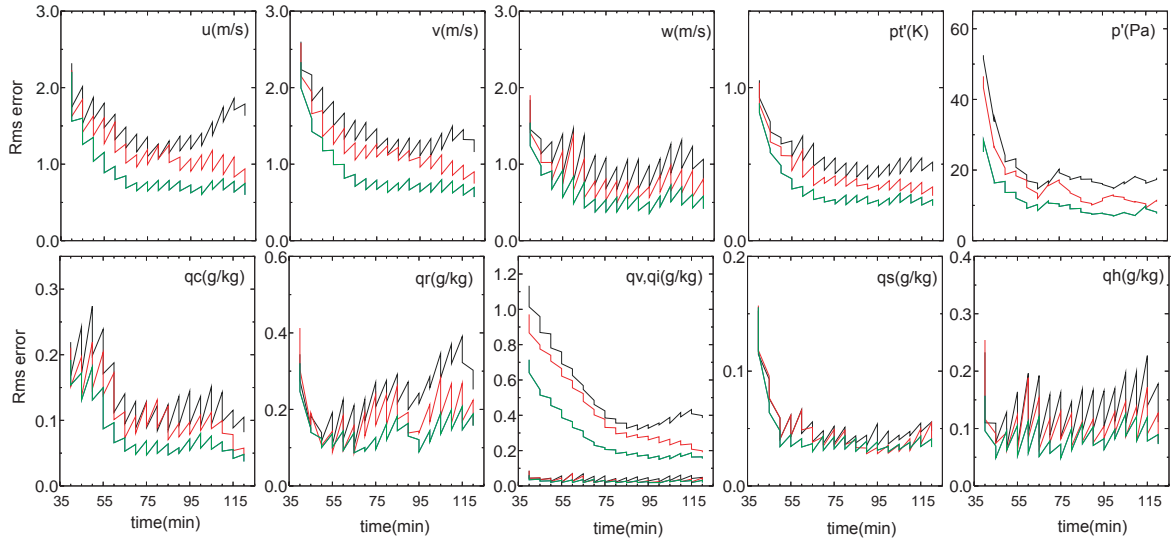
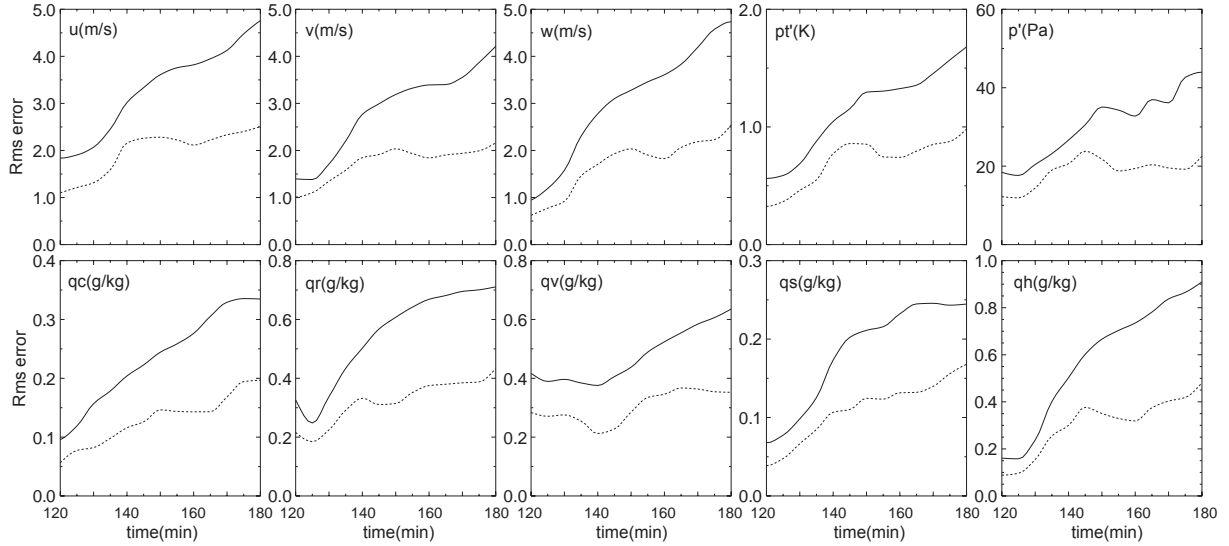Fig. 7. As Fig. 3, but for RAD115 (black), RASFCD115 (red) and RASFCD115S6 (green).

Fig. 8. The rms errors of ensemble mean forecasts from 120-min analyses of RA (solid) and RASFC (dotted), for a) u, b) v, c) w, d) θ, e) p, f) q_c, g) q_r, h) q_v and q_i, i) q_s, and j) q_h.

b) Varying surface observation spacing

Two other experiments are conducted to examine the impact of various surface network densities on the analysis. Surface network spacings of 20 km were used in the previous experiments (e.g., RASFC) while 12 km and 6 km are used in experiments RASFCS12 and RASFCS6 (Table 1). Their results are compared to those of RASFC. In these two experiments, surface observations are still uniformly distributed in the cen-

tral subdomain and there are 25 and 100 surface stations in RASFCS12 and RASFCS6, respectively.

In RASFCS12, for u, v, θ', p', q_v, q_c, q_r and q_s, the rms errors decrease faster and reached lower levels than in RASFC before 90 min (Fig. 6). After 90 minutes, as the splitting cell propagates quickly towards the northwest corner of small domain, the rms errors start to grow in RASFCS12 and become close to those of RASFC at the end of assimilation cycles since the number of surface observations covering part of the left

10

mover decrease. For q_r, the *rms* errors became slightly larger than those of RASFC during the later cycles.

When number of surface stations is increased to 100, with a 6 km spacing in RASFCS6, the errors for essentially all variables remain consistently lower than those of RASFC and RASFC12, especially during the later cycles. The improvement is similar to that of RASFC12 during the earlier cycles. These experiments demonstrate the benefit of having higher surface state densities, because of the high horizontal gradients in the surface features. For real storms that may contain even more small scale structures than the truth storm simulated at 2 km resolution, more benefit is expected of high density networks.

c) Varying radar location

In the next set of experiments, the radar is located closer to the storm, at a distance of 115 km in RAD115, RASFCD115 and RASFCD115S6, and a distance of 45 km in RADSFCD45 and RASFCD45S6.

Fig. 7 shows the *rms* errors of the first three experiments. With the radar at a close distance of 115 km, RA115 is able to produce much better analysis than RA, especially for the *u* velocity. The final levels of errors are lower, and the errors decrease faster during the initial cycles. In fact, the error peaks found in many variables in RA (Fig. 3) and other experiments of the same radar distance (Fig. 5 and Fig. 6) at round 60 min are mostly gone (Fig. 7). Obviously, the closer radar provides more low-level data coverage as well as a better vertical resolution at the location of the storm.

The impact of additional surface observations taken at 20 km spacings is smaller during the earlier assimilation cycles, compared to the 185 km case, but the impact increases during the later cycles (Fig. 7) partly because of the error increase in the non-surface data case (RAD115). This error increase may be because of the increasingly poorly analysis of the low-level wind and cold pool in the absence of low-level coverage while at the earlier times, the cold pool is smaller.

RASFCD115S6 produces a much more pronounced impact starting from the earlier cycles. After 90 min, the networks of both densities provide significant positive impact. We also observe that there is no degradation in the analyses of microphysical variables when more surface observations are added.

Compared with the improvement of RASFC over RA, RASFCD115 shows a generally comparable result at the end of assimilation cycles but a smaller impact early on. The *rms* error reductions of RASFCD115 over RAD115 for some variables are even slightly larger than those of RASFC over RA. This is an evidence that observations in the lowest km are still essential for ana-

lyzing detailed storm structures. The additional of surface data, even at a 20 km spacing, help alleviate the radar data coverage problem.

When radar is located much closer to the storm center with a distance of about 45 km, radar observations alone give much better results in terms of *rms* error; there is almost no room left for surface improvement by surface observations with 20 km spacings (not shown). The assimilation of surface observations as 6 km spacing in RASFCD45S6 improves the results only very slightly over RAD45 (not shown) The improve is in general insignificant. This is because the radar data have high horizontal and vertical resolutions and good coverage in this case, and the EnKF is very effective in analysis the data, especially when the assimilating model has no error.

5. Impact of surface observations on forecast

The ensemble mean analyses at 120 min from RA and RASFC are used as initial conditions to produce 60 min forecasts valid at 180 min. The forecast rms errors are plotted against time in Fig. 8. It can be seen that during the first 10 minutes or so of forecasts, the forecast error differences are maintained as similar levels as those in the initial conditions. After that, the differences start to increase with time. By the end of the 60 minute forecasts, the *rms* differences in *u*, *v* and *w* are more than 2 m s^{-1}, increasing from their initial values of 0.3 to 0.7 m s^{-1}, depending on the variables.

The error differences in most other fields more than double and for q_h the difference increases by a factor of about 7. These results indicate that the analysis error differences due to the use of surface observations, even at 20 km state spacings, are significant and the impact of surface data is amplified during the subsequent forecast.

An examination of the forecast reflectivity and divergence fields reveals that most of the enlarged *rms* error differences come from the propagation of the left moving cell (not shown). At 120 min, there is no distinct difference in the positions of the left mover between RA and RASFC but there are more errors in divergence field associated with the left moving cell near the northwest corner of the subdomain in RA than in RASFC. However, after 30 min of forecast, the left moving cell in RA propagates too fast and its center moved out of the subdomain. The difference is more evident in the divergence field, where the convergence and divergence centers related to the left mover totally disappear from the subdomain in RA. At 180 min, part of left moving cell remains on the boundary of subdomain in the truth simulation and in RASFC, there is no sign of it in RA.

11

7. Summary

In this paper, the ensemble square root Kalman filter is used to assimilate simulated radar and high-density surface network observations for a supercell convective storm, for the purpose of examining the impact of surface observations. It is found that use of mesonet-like surface observations can improve storm analysis over the ones using only radar observations. Surface observations help faster spin-up for the model to retrieve storm and display more accurate detail in analysis. In the following forecast, a better analysis obtained with both radar and surface observations also benefit numerical weather prediction. Among all 4 single surface observation types, wind shows the largest impact, which indicates the important role of low level convergence in storm generation, maintenance and propagation. Effect of various surface observation spacings and radar locations are also investigated. A denser surface observation network can improve analysis but not too much. When radar is closer to storm centre, surface observations also show some improvement until all low level information above the surface 100-200m is covered by radar observation.

Finally, we note here that the results obtained in this paper assume that the assimilating model is perfect. The impact of surface station data may not be the same when model errors are present. This is the topic of an ongoing study and we will report the results in a future paper.

References:

Brewster, K., 1996: Application of a Bratseth analysis scheme including Doppler radar data. Preprints, 15th Conf. Wea. Anal. Forecasting, Norfolk, VA, Amer. Meteor. Soc., 92-95.

Dawson, D. T., II and M. Xue, 2006: Numerical forecasts of the 15-16 June 2002 Southern Plains severe MCS: Impact of mesoscale data and cloud analysis. *Mon. Wea. Rev.*, **134,** 1607-1629.

Deng, X. and R. Stull, 2007: Assimilating surface weather observations from complex terrain into a high-resolution numerical weather prediction model *Mon. Wea. Rev.*, **135,** 1037–1054.

Doviak, R. and D. Zrnic, 1993: *Doppler Radar and Weather Observations*. 2nd ed. Academic Press, 562 pp.

Evensen, G., 2003: The ensemble Kalman filter: Theoretical formulation and practical implementation. *Ocean Dynamics*, **53,** 343-367.

Fujita, T., D. J. Stensrud, and D. C. Dowell, 2007: Surface data assimilation using an ensemble Kalman filter approach with initial condition and model physics uncertainties *Mon. Wea. Rev.*, In press.

Gaspari, G. and S. E. Cohn, 1999: Construction of correlation functions in two and three dimensions. *Quart. J. Roy. Meteor. Soc.*, **125,** 723-757.

Gilmore, M. S., J. M. Straka, and E. N. Rasmussen, 2004: Precipitation and evolution sensitivity in simulated deep convective storms: Comparisons between liquid-only and simple ice and liquid phase microphysics. *Mon. Wea. Rev.*, **132,** 1897-1916.

Hacker, J. P. and C. Snyder, 2005: Ensemble Kalman filter assimilation of fixed screen-height observations in a parameterized PBL. *Mon. Wea. Rev.*, **133,** 3260-3275.

Hacker, J. P. and D. Rostkier-Edelstrein, 2007: PBL state estimation with surface observations, a column model, and an ensemble filter. *Mon. Wea. Rev.*, Accepted.

Hong, S.-y. and J.-O. J. Lim, 2006: The WRF single-moment 6-class microphysics scheme (WSM6). *J. Korean Meteor. Soc.*, **42,** 129-151.

Jung, Y., G. Zhang, and M. Xue, 2007: Assimilation of simulated polarimetric radar data for a convective storm using ensemble Kalman filter. Part I: Observation operators for reflectivity and polarimetric variables. *Mon. Wea. Rev.*, Under reivew.

Lazarus, S., C. M. Ciliberti, J. D. Horel, and K. Brewster, 2002: Near-real-time applications of a mesoscale analysis system to complex terrain. *Wea. Forecast.*, **17,** 971-1000.

Lin, Y.-L., R. D. Farley, and H. D. Orville, 1983: Bulk parameterization of the snow field in a cloud model. *J. Climate Appl. Meteor.*, **22,** 1065-1092.

Liu, H. and M. Xue, 2007: Prediction of convective initiation and storm evolution on 12 June 2002 during IHOP. Part I: Control simulation and sensitivity experiments. *Mon. Wea. Rev.*, Conditionally accepted.

Lord, S. J., E. Kalnay, R. Daley, G. D. Emmitt, and R. Atlas, 1997: Using OSSEs in the design of the future generation of integrated observing systems. Preprint volume, 1st Symposium on Integrated Observation Systems, Long Beach, CA, Amer. Meteor. Soc., 45-47.

Meng, Z. and F. Zhang, 2007: Tests of an Ensemble Kalman Filter for Mesoscale and Regional-Scale

Data Assimilation. Part II: Imperfect Model Experiments *Mon. Wea. Rev.*, **135,** 1403–1423

Ray, P. S., B. Johnson, K. W. Johnson, J. S. Bradberry, J. J. Stephens, K. K. Wagner, R. B. Wilhelmson, and J. B. Klemp, 1981: The morphology of severe tornadic storms on 20 May 1977. *J. Atmos. Sci.*, **38,** 1643-1663.

Schultz, P., 1995: An explicit cloud physics parameterization for operational numerical weather prediction. *Mon. Wea. Rev.*, **123,** 3331-3343.

Tong, M. and M. Xue, 2005: Ensemble Kalman filter assimilation of Doppler radar data with a compressible nonhydrostatic model: OSS Experiments. *Mon. Wea. Rev.*, **133,** 1789-1807.

Tong, M. and M. Xue, 2007: Simultaneous estimation of microphysical parameters and atmospheric state with radar data and ensemble square-root Kalman filter. Part I: Sensitivity analysis and parameter identifiability *Mon. Wea. Rev.*, Conditionally accepted.

Weckwerth, T. M., D. B. Parsons, S. E. Koch, J. A. Moore, M. A. LeMone, B. B. Demoz, C. Flamant, B. Geerts, J. Wang, and W. F. Feltz, 2004: An overview of the International H2O Project (IHOP_2002) and some preliminary highlights. *Bull. Amer. Meteor. Soc.*, **85,** 253-277.

Whitaker, J. S. and T. M. Hamill, 2002: Ensemble data assimilation without perturbed observations. *Mon. Wea. Rev.*, **130,** 1913-1924.

Xue, M. and W. J. Martin, 2006: A high-resolution modeling study of the 24 May 2002 case during IHOP. Part I: Numerical simulation and general evolution of the dryline and convection. *Mon. Wea. Rev.*, **134,** 149–171.

Xue, M., K. K. Droegemeier, and V. Wong, 2000: The Advanced Regional Prediction System (ARPS) - A multiscale nonhydrostatic atmospheric simulation and prediction tool. Part I: Model dynamics and verification. *Meteor. Atmos. Physics*, **75,** 161-193.

Xue, M., M. Tong, and K. K. Droegemeier, 2006: An OSSE framework based on the ensemble square-root Kalman filter for evaluating impact of data from radar networks on thunderstorm analysis and forecast. *J. Atmos. Ocean Tech.*, **23,** 46–66.

Xue, M., Y. Jung, and G. Zhang, 2007: Error modeling of simulated reflectivity observations for ensemble Kalman filter data assimilation of convective storms. *Geophys. Res. Letters*, **34,** L10802, doi:10.1029/2007GL029945.

Xue, M., D.-H. Wang, J.-D. Gao, K. Brewster, and K. K. Droegemeier, 2003: The Advanced Regional Prediction System (ARPS), storm-scale numerical weather prediction and data assimilation. *Meteor. Atmos. Physics*, **82,** 139-170.

Xue, M., K. K. Droegemeier, V. Wong, A. Shapiro, K. Brewster, F. Carr, D. Weber, Y. Liu, and D.-H. Wang, 2001: The Advanced Regional Prediction System (ARPS) - A multiscale nonhydrostatic atmospheric simulation and prediction tool. Part II: Model physics and applications. *Meteor. Atmos. Phy.*, **76,** 143-165.

Zhang, F., C. Snyder, and J. Sun, 2004: Impacts of initial estimate and observations on the convective-scale data assimilation with an ensemble Kalman filter. *Mon. Wea. Rev.*, **132,** 1238-1253.

Zhang, F., Z. Meng, and A. Aksoy, 2006: Tests of an ensemble Kalman filter for mesoscale and regional-scale data assimilation. Part I: Perfect model experiments. *Mon. Wea. Rev.*, **134,** 722–736.